



REPORT - M2 COMPUPHYS

---

# Numerical Simulation of the Quantum Tunneling with the FDTD Method

---

Free Numerical Project

Hugo Alexandre

# Contents

<b>1</b>	<b>Introduction</b>	<b>2</b>
<b>2</b>	<b>Discretization of the Equations Using the FDTD Method</b>	<b>2</b>
2.1	Theoretical Definition . . . . .	2
2.2	The FDTD Method . . . . .	3
2.3	The Quantum Tunneling Effect . . . . .	4
<b>3</b>	<b>Alpha part - The 1D Quantum Tunneling Effect</b>	<b>4</b>
3.1	Code Initialization . . . . .	4
3.2	Numerical Resolution of the Schrödinger Equation . . . . .	5
3.3	Coherence and Validity of the Simulation . . . . .	5
3.3.1	Reflection and Transmission . . . . .	5
3.3.2	Mean Position and Deviation . . . . .	6
3.3.3	Phase Shift of the Wavefunction . . . . .	7
3.3.4	Hartman Time and Effect . . . . .	8
3.4	Conclusion . . . . .	9
<b>4</b>	<b>Beta part - The 2D Quantum Tunneling Effect</b>	<b>9</b>
4.1	Code Initialization and Numerical Resolution . . . . .	9
4.2	Coherence and Validity of the Simulation . . . . .	10
4.2.1	Reflection and Transmission Coefficients . . . . .	10
4.2.2	Mean Position and Deviation . . . . .	11
4.2.3	Hartman Effect in 2D . . . . .	11
4.3	Another representation of the 2D tunneling effect . . . . .	13
4.4	Conclusion . . . . .	13
<b>5</b>	<b>Golden part - The Quantum Double Slit Experiment</b>	<b>13</b>
5.1	Code Initialization and Numerical Resolution . . . . .	13
5.2	Coherence and Validity of the Simulation . . . . .	14
5.2.1	Study of $\lambda$ Dependence on Fringe Spacing . . . . .	15
5.2.2	Study of $D$ Dependence on Fringe Spacing . . . . .	16
5.2.3	Study of the Dependence of Slit Distance $d$ on Fringe Spacing . . . . .	16
5.2.4	Study of the Diffraction Pattern . . . . .	16
5.3	Alternative Representation of the Double-Slit with an Additional Dimension . . . . .	17
5.4	Conclusion . . . . .	17
<b>6</b>	<b>Platinum Part - Customizable 2D Potentials</b>	<b>17</b>
6.1	Potentials from a Drawing . . . . .	18
6.2	Potentials from an Image . . . . .	18
<b>7</b>	<b>Acknowledgements</b>	<b>18</b>
<b>8</b>	<b>Conclusion</b>	<b>19</b>

# Abstract

---

This project aims to simulate and visualize 2 main quantum phenomena, specifically quantum tunneling and Young's double-slit experiment, using numerical methods. The project is structured into three phases: the **Alpha** version simulates 1D quantum tunneling with a Gaussian wave packet, the **Beta** version extends the simulation to 2D tunneling, and the **Gold** version simulates the quantum double-slit experiment with still a Gaussian wavepacket. The simulations are implemented in **Python**, utilizing libraries such as **NumPy** for numerical computations and **Matplotlib** for dynamic visualizations.

---

## 1 Introduction

Quantum mechanics is one of the two major theories that revolutionized the 20th century, alongside the theory of General Relativity. It is known for describing the dynamics of the microscopic world and is particularly famous for the counterintuitive effects and phenomena it predicts, such as quantum tunneling and wave-particle duality (highlighted by the double-slit experiment). These phenomena, which are purely quantum, have no classical equivalent and will be the focus of this report. This project then seeks to simulate and visualize these phenomena using numerical methods.

The project is divided into three phases:

- **Alpha version:** Simulates the 1D quantum tunneling effect by modeling a Gaussian wave packet interacting with a potential barrier. This phase will provide an understanding of the tunneling process, including the visualization of reflection, transmission, and tunneling probability distributions, along with a theoretical analysis to validate the results.
- **Beta version:** Expands the simulation to 2D, enabling a more realistic spatial context. This phase involves discretizing 2D space and visualizing the probability density of the wave function across the grid using a colormap. Theoretical calculations will be performed to ensure the numerical results align with 2D theory.
- **Gold version:** Aims to simulate Young's double-slit experiment in a quantum framework. This phase will explore how slit width and spacing affect the diffraction pattern, aiming to generate the expected interference patterns numerically and verify that the theory matches the numerical results.

Each phase will be followed by a theoretical validation to ensure the accuracy of the simulation results. All parts of the project will use the Finite Difference Time Domain (FDTD) method to solve the time-dependent Schrödinger equation.

Additionally, I have introduced a "**Platinum**" version of the project, which allows users to custom potential by drawing it directly or to convert an image into a potential. However, no formal study will be conducted to verify the validity of this feature.

## 2 Discretization of the Equations Using the FDTD Method

In this section, we will define the problem with a theoretical approach and then present a numerical solution using the Finite Difference Time Domain (FDTD) method.

### 2.1 Theoretical Definition

We start by defining the problem through the fundamental equation of non-relativistic quantum mechanics: the Schrödinger equation. It is expressed as:

$$i\hbar \frac{\partial}{\partial t} \psi(\vec{r}, t) = \hat{H} \psi(\vec{r}, t), \quad (1)$$

where  $i$  is the imaginary unit such that  $i^2 = -1$ ,  $\hbar = h/2\pi$  is the reduced Planck constant,  $\psi(\vec{r}, t) \equiv \psi$  is the wave function describing the probability of finding a particle at position  $\vec{r}$  at time  $t$ .

The quantum Hamiltonian operator<sup>1</sup>  $\hat{H}$  is given by:

$$\hat{H} = \hat{T} + \hat{V}. \quad (2)$$

---

<sup>1</sup>A quantum operator is a linear application in Hilbert space that transforms  $\psi$  within this space.

It represents the energy of the system and governs the evolution of the associated wave function. The operator  $\hat{T}$  corresponds to the kinetic energy, while  $\hat{V}$  is the potential energy.

Since we consider only non-relativistic cases ( $v \ll c$ ), the kinetic energy  $T$  is defined as:

$$T = \frac{|\vec{p}|^2}{2m}, \quad (3)$$

where  $\vec{p}$  is the momentum and  $m$  is the mass of the particle. According to Bohr's correspondence principle, the momentum operator  $\vec{p}$  is given by:

$$\vec{p} \iff -i\hbar\vec{\nabla}. \quad (4)$$

By substituting this into Eq.(3), the Hamiltonian operator becomes:

$$\hat{H} = -\frac{\hbar^2}{2m}\vec{\nabla}^2 + \hat{V}. \quad (5)$$

Thus, the Schrödinger equation we will use in the subsequent sections is:

$$i\hbar\frac{\partial}{\partial t}\psi(\vec{r}, t) = -\frac{\hbar^2}{2m}\vec{\nabla}^2\psi(\vec{r}, t) + \hat{V}\psi(\vec{r}, t). \quad (6)$$

Eq.(6) provides the spatial and temporal evolution of a wave packet  $\psi$  based on the characteristics of the system, as modeled by the potential  $\hat{V}$ .

## 2.2 The FDTD Method

The Finite-Difference Time-Domain (FDTD) method is a powerful numerical approach for solving partial differential equations (PDEs), including the Schrödinger equation (Eq.6), in complex geometries. By discretizing both space and time, it allows the simulation of a wavepacket<sup>2</sup> and its interaction with the environment.

To apply the FDTD method, the Schrödinger equation is converted from its continuous form into a finite-difference representation, enabling numerical computation. This transformation is important for modeling the evolution of the wavefunction of a quantum particle.

However, instead of directly discretizing Eq.(6), we first decouple it. Indeed, since  $\psi \in \mathbb{C}$ , it can be expressed as  $\psi \rightarrow \Re(\psi) + i\Im(\psi)$ , where the wavefunction

$\psi$  is separated into its real part  $\Re(\psi) = \psi_R$  and imaginary part  $\Im(\psi) = \psi_I$  such that  $\psi^2 = \psi_R^2 + \psi_I^2$ . This leads to the following system of 2 real equations:

$$\hbar\frac{\partial\psi_R}{\partial t} = -\frac{\hbar^2}{2m}\nabla^2\psi_I + V\psi_I, \quad (7)$$

$$\hbar\frac{\partial\psi_I}{\partial t} = \frac{\hbar^2}{2m}\nabla^2\psi_R - V\psi_R. \quad (8)$$

This system will be easier to solve than using the imaginary equation, which Python has trouble handling. Next, we discretize these equations in both space and time. For the 2D case, we define the wavefunction  $\psi(x, y, t)$  at discrete points as  $\psi(x, y, t) \rightarrow \psi_{i,j}^n$ , where  $n \rightarrow t$  corresponds to the time step, and  $(i, j) \rightarrow (x, y)$  are the spatial coordinates.

The differential operators are discretized as follows:

$$\frac{\partial\psi}{\partial t} \rightarrow \frac{\psi_{i,j}^{n+1} - \psi_{i,j}^n}{\Delta t}, \text{ where } \Delta t \text{ is the time step.}$$

$$\frac{\partial^2\psi}{\partial x^2} \rightarrow \frac{\psi_{i+1,j}^n - 2\psi_{i,j}^n + \psi_{i-1,j}^n}{\Delta x^2}, \text{ where } \Delta x \text{ is the spatial step in } x.$$

$$\frac{\partial^2\psi}{\partial y^2} \rightarrow \frac{\psi_{i,j+1}^n - 2\psi_{i,j}^n + \psi_{i,j-1}^n}{\Delta y^2}, \text{ where } \Delta y \text{ is the spatial step in } y.$$

Substituting these expressions into Eqs.(7) and (8), we obtain the following coupled, discretized equations:

$$\hbar\frac{\psi_{R,i,j}^{n+1} - \psi_{R,i,j}^n}{\Delta t} = \frac{-\hbar^2}{2m}(D_i^2 + D_j^2)\psi_{I,i,j}^n + V\psi_{I,i,j}^n \quad (9)$$

$$\hbar\frac{\psi_{I,i,j}^{n+1} - \psi_{I,i,j}^n}{\Delta t} = \frac{\hbar^2}{2m}(D_i^2 + D_j^2)\psi_{R,i,j}^n - V\psi_{R,i,j}^n \quad (10)$$

$$\text{where } D_i^2 + D_j^2 = \frac{\psi_{R/I,i+1,j}^n - 2\psi_{R/I,i,j}^n + \psi_{R/I,i-1,j}^n}{\Delta x^2} + \frac{\psi_{R/I,i,j+1}^n - 2\psi_{R/I,i,j}^n + \psi_{R/I,i,j-1}^n}{\Delta y^2}$$

As time is discretized into small intervals  $\Delta t$ , the temporal resolution is crucial as it influences the stability of the simulation. The relationship between the spatial step sizes and the time step is governed by the

---

<sup>2</sup>Group of superposed waves forming a localized traveling disturbance

Courant-Friedrichs-Lowy (CFL) condition [1], which ensures that the numerical wavepacket propagation does not exceed the grid size in a single time step.

In practical terms, the CFL condition establishes a constraint between the spatial and temporal discretizations. Specifically, it ensures that the time step  $\Delta t$  is sufficiently small relative to the spatial step sizes  $\Delta x$  and  $\Delta y$ , to prevent numerical instabilities. The relationship can be expressed as:

$$\Delta t \leq \alpha \frac{2m}{\hbar} \frac{\Delta x \Delta y}{\sqrt{\Delta x^2 + \Delta y^2}}, \quad (11)$$

where  $\alpha \ll 1$  is a proportionality factor ensuring that the condition is satisfied for the chosen discretization scheme.

To update the wave functions  $\psi_R$  and  $\psi_I$  at each time step  $\Delta t$ , we need to calculate  $\psi_{R,i,j}^{n+1}$  and  $\psi_{I,i,j}^{n+1}$  from Eqs. (9, 10). The updated expressions for these wave functions, derived from the discretized equations, are given by Eqs. (12, 13):

$$\psi_{R,i,j}^{n+1} = \psi_{R,i,j}^n - \frac{\hbar}{2m} \Delta t (D_i^2 + D_j^2) \psi_{I,i,j}^n + \frac{\Delta t}{\hbar} V \psi_{I,i,j}^n \quad (12)$$

$$\psi_{I,i,j}^{n+1} = \psi_{I,i,j}^n + \frac{\hbar \Delta t}{2m} (D_i^2 + D_j^2) \psi_{R,i,j}^n - \frac{\Delta t}{\hbar} V \psi_{R,i,j}^n \quad (13)$$

## 2.3 The Quantum Tunneling Effect

The tunneling effect is a quantum phenomenon that allows a particle to traverse a potential barrier even when its energy is lower than the height of the barrier [10]. This phenomenon, which is impossible in classical physics, has significant implications in various fields, such as nuclear physics, semiconductor physics, and scanning tunneling microscopy.

In our study, we consider a quantum box<sup>3</sup> of size  $L = 5$ , within which there is a potential barrier  $V(x)$  of width  $a$  located at position  $L/2$ . The potential  $V(x)$  is defined as:

$$V(x) = \begin{cases} V_0 & \text{if } x \in [\frac{L-a}{2}, \frac{L+a}{2}] \\ 0 & \text{otherwise} \end{cases} \quad (14)$$

<sup>3</sup>A quantum box is defined as a region where  $V = \infty$  at  $x = 0$  and  $x = L$ .

The scenario is illustrated in Fig. 1.

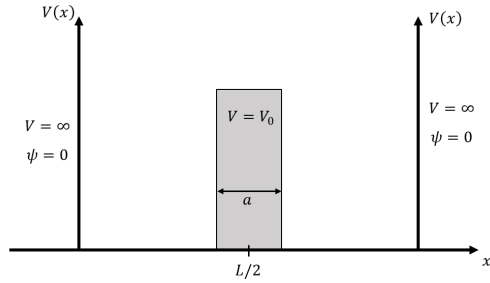


Figure 1: 1D Quantum box with a potential barrier

As previously mentioned, if a particle with energy lower than the potential height approaches the barrier, it has a non-zero probability of crossing it. From a quantum perspective, this means that a portion of the wave function associated with the particle can penetrate and pass through the barrier.

## 3 Alpha part - The 1D Quantum Tunneling Effect

### 3.1 Code Initialization

To build our code, we begin with the initialization of the problem. We consider a quantum box of size  $L = 5$  nm and a potential barrier with height  $V_0 = 80$  eV and width  $a = 70$  pm.

We initialize a Gaussian wavepacket with a de Broglie wavelength  $\lambda = 1.5 \times 10^{-10}$  m, propagating with a momentum  $\hbar k$ , where  $k = \frac{2\pi}{\lambda}$ . The initial wave function is given by:

$$\psi_0(x) = e^{-\frac{1}{2} \frac{(x-x_0)^2}{\sigma^2}} e^{ik(x-x_0)} \quad (15)$$

Here, we set  $x_0 = L/4$  and  $\sigma = 2.0 \times 10^{-10}$  m.

The term  $k > 0$  represents the wave function's velocity, which depends on  $\lambda$ , and describes its motion towards positive  $x$ -direction. Since the wave function must be normalized (which is not initially the case), the normalization will be handled during the computation of the Schrödinger equation. However, recall that our

wave function is coupled into two equations for the real and imaginary parts. Thus, Eq. (15) can be rewritten as:

$$\psi_{0,R}(x) = e^{-\frac{1}{2} \frac{(x-x_0)^2}{\sigma^2}} \cos(k(x-x_0)) \quad (16)$$

$$\psi_{0,I}(x) = e^{-\frac{1}{2} \frac{(x-x_0)^2}{\sigma^2}} \sin(k(x-x_0)) \quad (17)$$

We note that the relationship  $\psi^2 = \psi_R^2 + \psi_I^2$  holds. Furthermore, we can deduce the kinetic energy  $E_k$  of the particle using from the Eq.(3) which gives us Eq.(18):

$$E_k = \frac{\hbar^2 k^2}{2m} \quad (18)$$

This yields a kinetic energy  $E_k = 66.85 \text{ eV} < V_0$ .

### 3.2 Numerical Resolution of the Schrödinger Equation

In this section, we briefly explain the numerical method used to solve the decoupled Schrödinger equations (Eqs. 7, 8) at each time step  $\Delta t$ , following the CFL condition in Eq. (11) with  $\alpha = 0.1$ , ensuring the stability of the simulation.

The potential  $V(x)$  is defined numerically as follows:

```
barrier_start = L/2 - a/2
barrier_end = L/2 + a/2
U0 = 80 # Barrier height in eV
U = np.zeros(Nx) # Initialize potential array
U[(x >= barrier_start) &
(x <= barrier_end)] = U0
```

Next, we compute the updated wave functions  $\psi_R(x)$  and  $\psi_I(x)$  at each time step using the finite difference method:

```
for _ in range(60): # Iterate over time steps
    Psi_Real[1:-1] = Psi_Real[1:-1]
    - a2 * (Psi_Img[2:] - 2 * Psi_Img[1:-1]
    + Psi_Img[:-2])
    + a3 * U[1:-1] * Psi_Img[1:-1]

    Psi_Img[1:-1] = Psi_Img[1:-1]
    + a2 * (Psi_Real[2:] - 2 * Psi_Real[1:-1]
    + Psi_Real[:-2])
    - a3 * U[1:-1] * Psi_Real[1:-1]
```

```
Psi_Prob[1:-1] = Psi_Real[1:-1]**2
+ Psi_Img[1:-1]**2
```

After updating, we normalize the wave function as follows:

$$\psi_R \rightarrow \frac{\psi_R}{\sqrt{\int_0^L \psi_{\text{Prob}}^2 dx}}, \quad \psi_I \rightarrow \frac{\psi_I}{\sqrt{\int_0^L \psi_{\text{Prob}}^2 dx}} \quad (19)$$

where  $\psi_{\text{Prob}} = \sqrt{\psi_R^2 + \psi_I^2}$  ensures the conservation of probability.

Finally, running the simulation produces the results shown in Fig.2 where we can see the quantum nature of the wave function when it crosses the barrier, the reflected part only takes on a certain discrete value which appears as a hatched area.

### 3.3 Coherence and Validity of the Simulation

In this section, we will study the coherence of our model by comparing some numerical results with theoretical predictions.

#### 3.3.1 Reflection and Transmission

As the wave function passes through the potential barrier, as shown in Fig.2, we focus on the transmission coefficient  $T$  and the reflection coefficient  $R$ .

Theoretically, the transmission and reflection coefficients are given by Eqs.(20, 21), based on [10]:

$$T = \frac{1}{1 + \frac{V_0^2}{4E_k(V_0-E_k)} \sinh^2(Ka)} \quad (20)$$

$$R = \frac{\frac{V_0^2}{4E_k(V_0-E_k)} \sinh^2(Ka)}{1 + \frac{V_0^2}{4E_k(V_0-E_k)} \sinh^2(Ka)} \quad (21)$$

$$\text{where } K = \frac{\sqrt{2m(V_0 - E_k)}}{\hbar}.$$

It can be verified that  $T + R = 1$ , which reflects the relation  $\psi^2 = \psi_{\leftarrow}^2 + \psi_{\rightarrow}^2 = 1$ . This indicates that the total wave function is composed of two components: one on the left side of the barrier and the other on the right. This implies that the right part  $\psi_{\rightarrow}$  corresponds

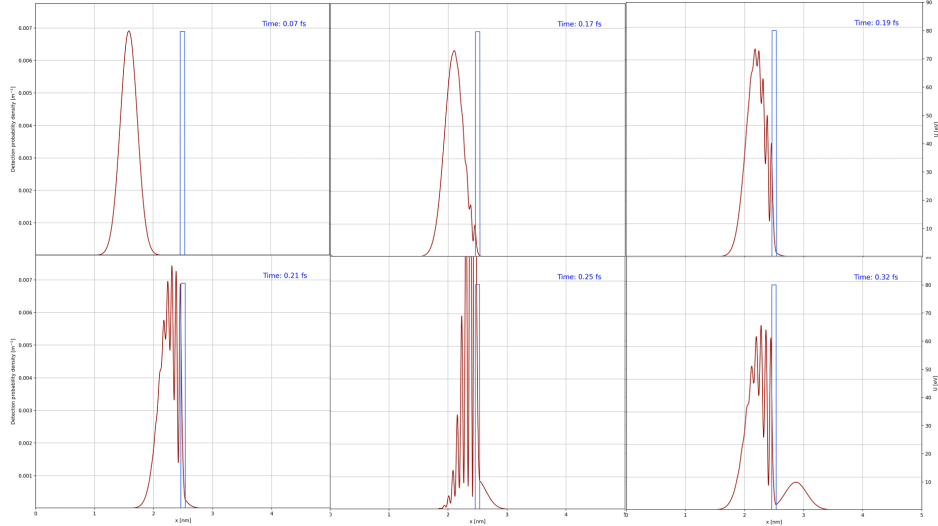


Figure 2: Simulation of the 1D tunneling effect observed at different time steps. Animation of the effect associated with this figure provided in the Alpha file named ‘QT\_1D’.

to the transmission coefficient  $T$ , and the left part  $\psi_{\leftarrow}$  corresponds to the reflection coefficient  $R$ :

$$\psi_{\rightarrow}^2 = T \quad (22)$$

$$\psi_{\leftarrow}^2 = R \quad (23)$$

We can plot the transmission coefficient and the probabilities  $\psi_{\rightarrow}^2$  and  $\psi_{\leftarrow}^2$  as functions of time. The results are shown in Fig.3:

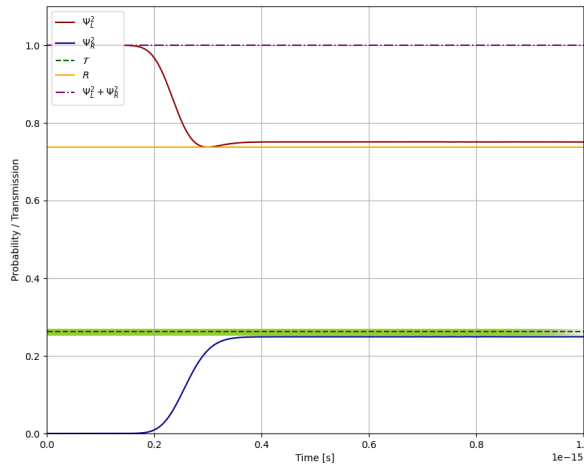


Figure 3: Comparison between the transmission/reflection coefficient and the probability densities in a 1D quantum box with a potential barrier.

We observe that the numerical transmission coefficient  $\psi_{\rightarrow}^2$  matches closely with the theoretical value  $T$ ,

and similarly for  $\psi_{\leftarrow}^2$  and  $R$ . The green curve represents the relative error between  $T$  and  $\psi_{\rightarrow}^2$ .

The results in Fig.3 demonstrate that the numerical and theoretical results are in good agreement.

Additionally, the fact that the total wave function satisfies  $\psi^2 = \psi_{\leftarrow}^2 + \psi_{\rightarrow}^2 = 1$  at every time step  $\Delta t$  supports the consistency of the simulation. Since the energy of the system is given by Eq.(24):

$$E_{\text{tot}} = \int_0^L \left[ -\frac{\hbar^2}{2m} |\vec{\nabla} \psi(x, t)|^2 + V(x) |\psi(x, t)|^2 \right] dx \quad (24)$$

and depends only on the wave function, we can confirm that the energy of the system is conserved, as the wave function remains normalized without divergence.

### 3.3.2 Mean Position and Deviation

We will focus on the deviation and the mean position of the wavefunction.

The mean position and quantum deviation are given by the following equations:

$$\langle x \rangle = \int_0^L x |\psi(x, t)|^2 dx \quad (25)$$

$$\sigma_x = \sqrt{\int_0^L x^2 |\psi(x, t)|^2 dx} \quad (26)$$

We can plot the mean position and the deviation as functions of time and compare them with a theoretical average. However, the form of  $\psi^2$  is no longer analytic,

so we need to approach this differently. One method is to track the maximum of the wavefunction and plot it as a function of time. Since the wavefunction corresponds to a Gaussian wave packet, the mean and the maximum should coincide. Therefore, we expect the two curves to overlap, we then plot the different quantities, as shown in Fig.4.

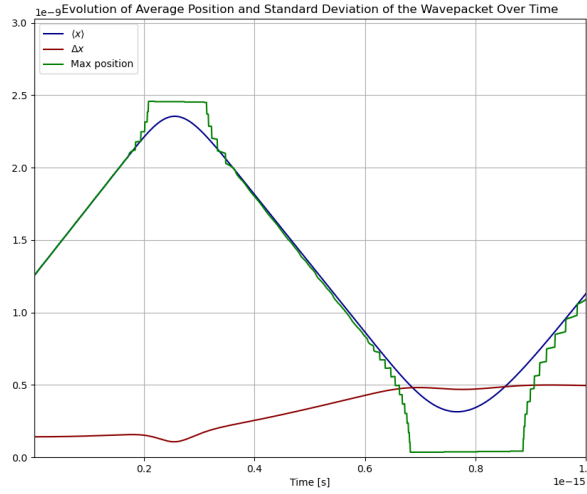


Figure 4: Mean position and deviation compared to the theoretical maximum of the position calculated.

We observe that up to 0.2 fs, the mean position and the maximum position overlap, validating the coherence of our simulation up to that point.

Beyond this time, we notice a stair-step pattern corresponding to the discretization of  $\psi^2$ , a quantum behavior, visible in Fig.2. Despite this discrete structure, the trend between the maximum position and  $\langle x \rangle$  seems to align well. However, I have not performed the same analysis for the deviation, but we might expect similar results.

### 3.3.3 Phase Shift of the Wavefunction

In this section, we analyze the phase shift caused by the potential barrier on the wavefunction.

As the wavefunction propagates, its phase evolves over time.

In a simplified model, to a first approximation, the theoretical phase shift  $\varphi_{th}$  depends on the energy  $E_k$ , as described in Eq.(18), and can be expressed as:

$$\varphi_{th} = \frac{E_k}{\hbar} t \quad (27)$$

However, this equation does not account for the complex interactions between the wavefunction and the potential barrier [10]. As a result, we expect a behavior that deviates from what is predicted by Eq.(27).

On the other hand, the numerical phase shift of the wavefunction is described by:

$$\varphi_{num} = \arctan 2(\psi_I, \psi_R) \quad (28)$$

When plotting the two phase shifts,  $\varphi_{th}$  and  $\varphi_{num}$ , we obtain Fig.5.

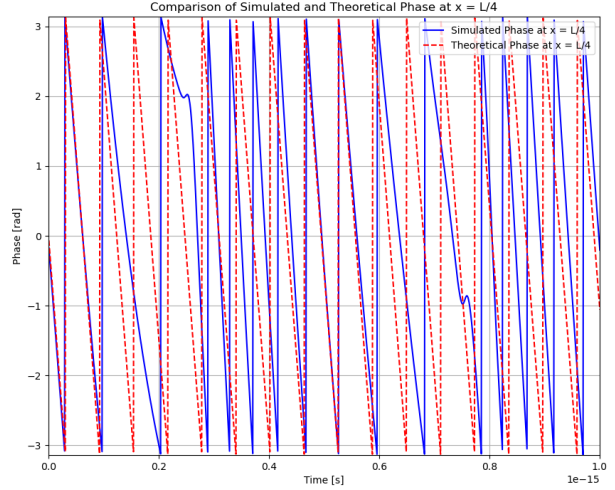


Figure 5: Theoretical and numerical phase shift of the wavefunction as a function of time.

As previously mentioned, the numerical phase shift initially follows the theoretical phase shift. However, over time, we observe a divergence, leading to behavior that no longer aligns with the expectations given by Eq.(27).

A specific behavior of the numerical phase shift is observed around  $t \approx 0.25$  fs, corresponding to the wavefunction's reflection off the potential barrier (while part of it is transmitted). Subsequently, we observe a realignment of the phase, which occurs around  $t \approx 0.5$  fs, when the wavefunction reflects off the walls of the quantum box.

### 3.3.4 Hartman Time and Effect

This section concludes with the traversal time and a brief study of the Hartman time.

In the first approximation, for large widths, we can assume that the traversal time is given by Eq.(29).

$$\tau = \frac{\hbar}{(V_0 - E_k)e} \quad (29)$$

The calculated time is approximately  $\tau \approx 0.36$  fs, which is in good agreement with the simulated time, as shown in Fig.6.

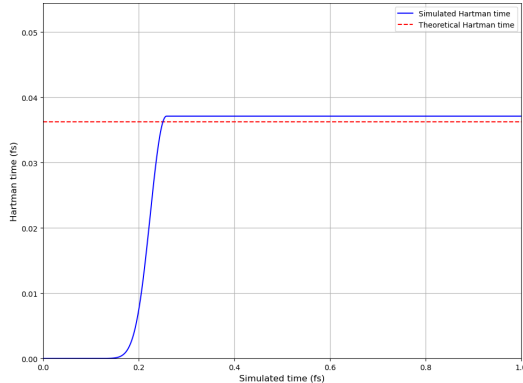


Figure 6: Theoretical traversal time compared with the numerical traversal time of the wavefunction in a potential barrier

We notice that the times align reasonably well, though a study on the relative errors would provide more insight into these results.

However, the Hartman effect extends much further and posits that the tunneling time is independent of the barrier width  $a$  [5, 6, 4].

This result implies that tunneling could involve superluminal speeds, as if the particle described by the matter wave travels faster than the speed of light.

The formula for Hartman time in the non-relativistic regime is given from [12] by Eq.(30).

$$\tau_h = \frac{mk}{\hbar|d|^2} \left[ \frac{k^2 + K^2}{kK} \sinh(2Ka) - 2ka(k^2 - K^2) \right] \quad (30)$$

where  $|d|^2 \equiv |d(k, K, a)|^2 = [(k^2 - K^2) \sinh(Ka)]^2 + [2kK \cosh(Ka)]^2$ ,  $k = \frac{\sqrt{2mE_k}}{\hbar}$  and  $K = \frac{\sqrt{2m(V_0-E_k)}}{\hbar}$ .

These quantities only depend on the potential and the kinetic energy. For  $V_0 = 80$  eV and  $E_k = 66.85$  eV fixed, we can plot the Hartman time (i.e., the traversal time of the barrier) as a function of the width  $a$ , which gives the result<sup>4</sup> shown in Fig.7.

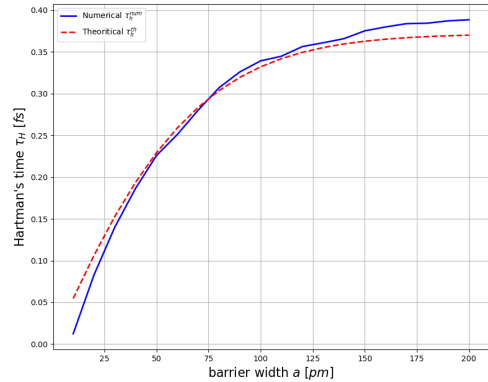


Figure 7: Traversal time of the Gaussian wave packet in the potential barrier as a function of its width  $a$  [5]

Indeed, we observe a temporal convergence in the data, highlighting the well-known Hartman effect [5] and Fig.7 illustrates this effect and also shows that our simulation seems to adhere well to the underlying physics.

Regarding this effect, a more plausible explanation proposed by [3] suggests that the wave packet reshapes during tunneling. The initial parts of the packet are less attenuated than the later parts, which causes the center of the packet to shift forward, giving the impression of a faster arrival.

This effect is counterbalanced by the exponential decay of the signal during the tunneling process, meaning that the probability of detecting the particle decreases significantly. This phenomenon has been analyzed [8] to show that the tunneling effect does not violate relativity, as the faster speed comes with a reduced intensity.

We estimated the precision and validity of our numerical and theoretical data by plotting the correlation graph in Fig.8, highlighting the  $R^2$  term.

<sup>4</sup>The numerical points were obtained by calculating the time difference when the quantum mean reaches a minimum on the left (reflection) and rises rapidly on the right (transmission) for several width values  $a$

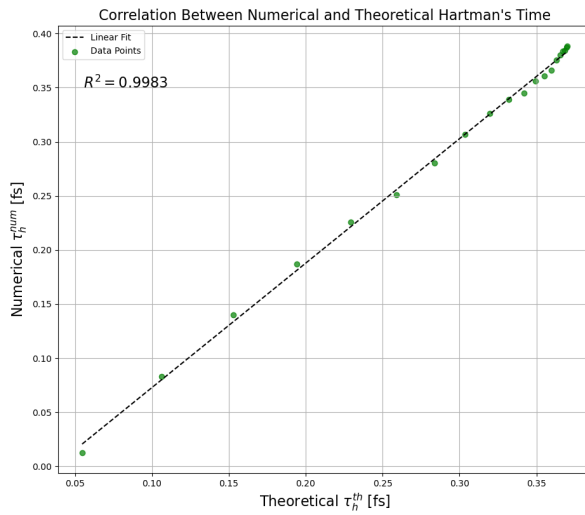


Figure 8: Correlation graph between numerical and theoretical values, highlighting an  $R^2$  close to 1

Fig.8 shows a strong correlation of  $R^2 = 0.9983$  between the numerical and theoretical data, confirming the validity of the numerical simulations of the 1D tunneling effect.

### 3.4 Conclusion

The analysis of the **Alpha** part confirms that the numerical model aligns with the theoretical model on several aspects, such as the average results, the Hartman effect, and the conservation of mechanical energy.

These results attest to the validity and accuracy of the simulation in modeling the quantum tunneling effect.

## 4 Beta part - The 2D Quantum Tunneling Effect

Once the **Alpha** part was completed, the transition to the **Beta** version was straightforward by leveraging the same principles. The **Alpha** version was adapted to 2D using numerical tools.

### 4.1 Code Initialization and Numerical Resolution

In this part, we update our quantum system, which is now a 2D quantum box (Fig.9) of size  $L_x \times L_y$  (where  $L_x = L_y = L$ ) with a potential  $V_0 = 70$  eV, and a barrier width along the  $x$ :  $a = 50$  pm.

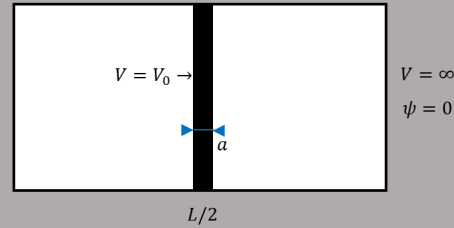


Figure 9: 2D Quantum Box with a barrier (black) of width  $a$

The initial 2D wave function is adjusted relative to the one described in Eq.(15) :

$$\psi_0(x, y) = e^{-\frac{(x-x_0)^2}{2\sigma_x^2}} e^{ik(x-x_0)} e^{-\frac{(y-y_0)^2}{2\sigma_y^2}} \quad (31)$$

The code from the previous section is adapted to 2D by discretizing Eq(9, 10) in a loop. After applying the necessary modifications, we initialize the parameters as follows:

```
# Constants and simulation parameters
Lx, Ly = 5.0e-9, 5.0e-9
x0, y0 = Lx / 4, Ly / 2 # initial position
sigma_x, sigma_y = 2.0e-10, 2.0e-10 # width
Lambda = 1.5e-10 # de Broglie wavelength
U0 = 70 # potential
a = 5e-11 # barrier width
center_x, center_y = Lx / 2, Ly / 2
U = np.zeros((Ny, Nx))
U[(X >= center_x - a / 2) &
(X <= center_x + a / 2)] = U0 # 2D barrier
```

The 2D wave function is updated every 6 time steps to speed up the simulation while maintaining sufficient accuracy (the time step is small enough to make this

optimization visually negligible). The update loop is as follows:

```

for i in range(skip_frame):
    # Calculate the finite difference for the
    # wave function evolution
    Psi_Real[1:-1, 1:-1] = Psi_Real[1:-1, 1:-1]
    - alpha * ((Psi_Img[2:, 1:-1]
    - 2 * Psi_Img[1:-1, 1:-1] +
    Psi_Img[:-2, 1:-1]) / dx2
    + (Psi_Img[1:-1, 2:] -
    2 * Psi_Img[1:-1, 1:-1] +
    Psi_Img[1:-1, :-2]) / dy2)
    + A2 * U[1:-1, 1:-1] * Psi_Img[1:-1, 1:-1]

    Psi_Img[1:-1, 1:-1] = Psi_Img[1:-1, 1:-1]
    + alpha * ((Psi_Real[2:, 1:-1]
    - 2 * Psi_Real[1:-1, 1:-1]
    + Psi_Real[:-2, 1:-1]) / dx2
    + (Psi_Real[1:-1, 2:] - 2 *
    Psi_Real[1:-1, 1:-1] + Psi_Real[1:-1, :-2])
    / dy2) - A2 * U[1:-1, 1:-1]
    * Psi_Real[1:-1, 1:-1]

    # Update probability density
    Psi_Prob = (Psi_Real**2 + Psi_Img**2)

```

The indices within the square brackets select specific regions of the grid for calculating second-order derivatives using the FDTD:

- `[1:-1, 1:-1]` : The main grid area, excluding the edges, where the updates are performed.
- `[:-2, 1:-1]` : Elements located one cell **above** ( $y - 1$ ) the main grid area along the vertical axis.
- `[2:, 1:-1]` : Elements located one cell **below** ( $y + 1$ ) the main grid area along the vertical axis.
- `[1:-1, :-2]` : Elements located one cell **to the left** ( $x - 1$ ) of the main grid area along the horizontal axis.
- `[1:-1, 2:]` : Elements located one cell **to the right** ( $x + 1$ ) of the main grid area along the horizontal axis.

The real and imaginary parts of the wave function are normalized using the same method as described in Eq.(19). The result of the simulation gives us the Fig.10.

In Fig.10, we observe the discrete nature of the Gaussian wave packet near the 2D barrier, where it takes on specific discrete values. Further details of this behavior will be explored in the next section.

## 4.2 Coherence and Validity of the Simulation

In this section, in the same way as before, we will analyse the validity of our 2D model by simulating several effects resulting from the tunnel effect and comparing them with the theoretical aspects already known.

### 4.2.1 Reflection and Transmission Coefficients

As in the **Alpha part**, we focus on the reflection and transmission coefficients  $R$  and  $T$ , determined by Eqs.(20, 21).

Given that we consider a Gaussian wavepacket propagating along the positive  $x$ -direction, as described by Eq.(31), we expect results similar to those shown in Fig.11. By determining the wave function on the left and right sides of the barrier and plotting them as functions of time, we obtain Fig.11.

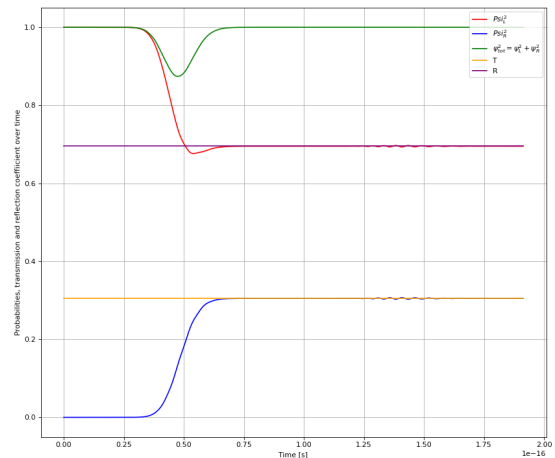


Figure 11: Reflection  $R$  and transmission  $T$  coefficients, as well as the left and right wave functions plotted as functions of time in the 2D tunneling model.

In Fig.11, we observe that the values of  $\psi_{\leftarrow}^2$  and  $R$  are relatively close, as are those of  $\psi_{\rightarrow}^2$  and  $T$ . This implies that the total wave function  $\psi^2 = \psi_{\leftarrow}^2 + \psi_{\rightarrow}^2$  is conserved

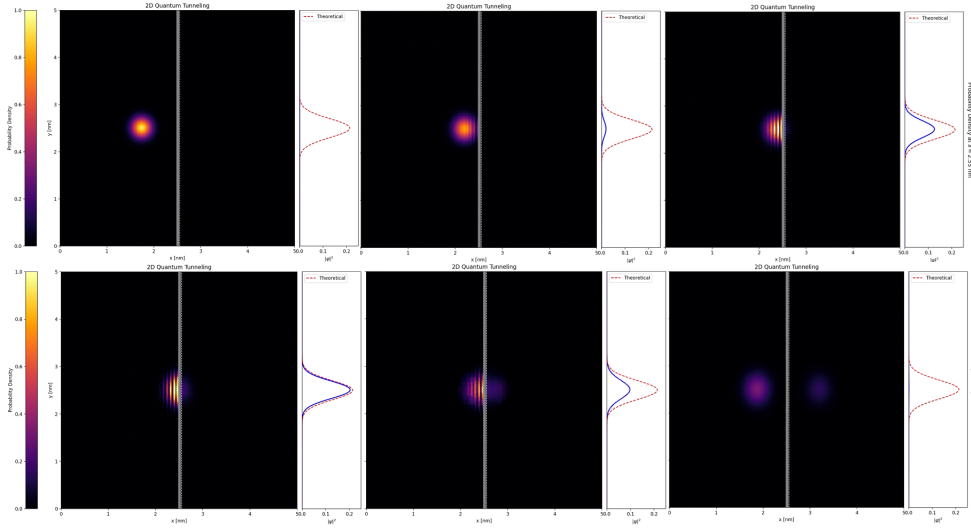


Figure 10: Simulation of the 2D tunneling effect observed at different time steps with the profil wave function. Animation of the effect associated with this figure provided in the Beta file named ‘QT\_2D’.

over the entire quantum box. According to Eq.(24), this means that the energy (calculable in 2D) only depends on the wave function. Thus, if  $\iint_{[0,L]^2} |\psi|^2 dx dy$  always equals 1, the energy is conserved.

However, we notice that  $|\psi|^2 \neq 1$  around  $t \approx 0.45$  fs. This discrepancy arises from the way the left and right wave functions are defined. These functions are only defined in the regions where  $V_0 = 0$ , to the left and right of the barrier, but not inside it. This variation is due to the fact that  $|\psi|^2 \neq 0$  within the barrier, but this contribution is not accounted for. Since the wave function’s amplitude decreases exponentially,  $|\psi|^2$  quickly approaches or equals 1 again shortly thereafter.

#### 4.2.2 Mean Position and Deviation

In this section, we compute the mean position and the deviation of our wave function as a function of time, for both the  $x$  and  $y$  coordinates.

For the same reason introduced previously, as the wave packet only propagates along the  $x$ -axis, we expect results similar to those shown in Fig.4 for the  $x$ -coordinate, and a constant mean position  $\langle y \rangle = y_0$  in the  $y$ -direction.

The mean positions are calculated using Eq.(25), while the deviations are obtained via Eq.(26). The maximum positions are determined in the same manner as for the 1D case. The results are plotted as functions of time in Fig.12.

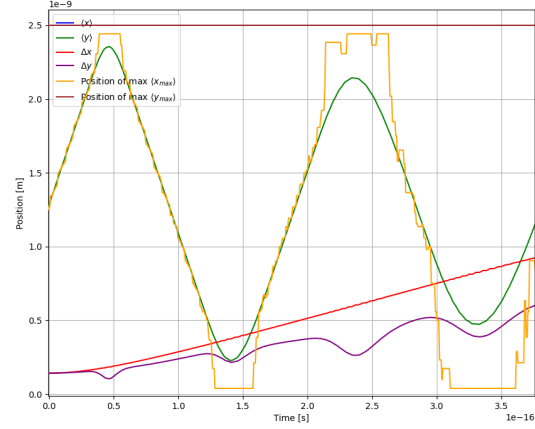


Figure 12: Numerical and theoretical mean positions and deviations in  $x$  and  $y$  for the 2D model.

As expected, the mean position  $\langle y \rangle$  remains constant at  $y_0 = L/2$ , corroborated by the behavior of  $y_{\max}$ . For the  $\langle x \rangle$ , we observe a behavior very similar to that in Fig.4.

Additionally, the deviations in both  $x$  and  $y$  exhibit a quasi-linear growth, attributed to the spreading of the wave packet during its propagation.

#### 4.2.3 Hartman Effect in 2D

In this section, we study the Hartman effect in 2D and verify whether our 2D model reproduces the same results as the numerical 1D model, which operates based on the results shown in Fig.8.

We will validate our 2D results using the same type of analysis.

First, we determine the traversal time of a particle with parameters  $V_0 = 85$  eV and  $a = 75$  pm and plot it, yielding Fig.13.

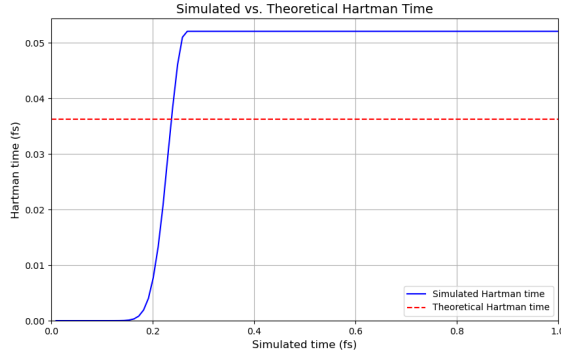


Figure 13: Theoretical and numerical traversal time of the wave function in 2D.

In Fig.13, we observe behavior similar to that in Fig.6, from the value toward which  $\tau_H$  converges. For these values of  $V_0$  and  $a$ , we expect results similar with the 1D case. Even if the result is not the same between the 1D and 2D case, it remains in the same order of magnitude, with a relative error of  $\delta\tau_H \approx 44\%$ , showing a discernible trend. Increasing the number of points would improve accuracy but would significantly increase computation time.

For various barrier widths  $a$ , we can plot the Hartman time curve (Fig.14).

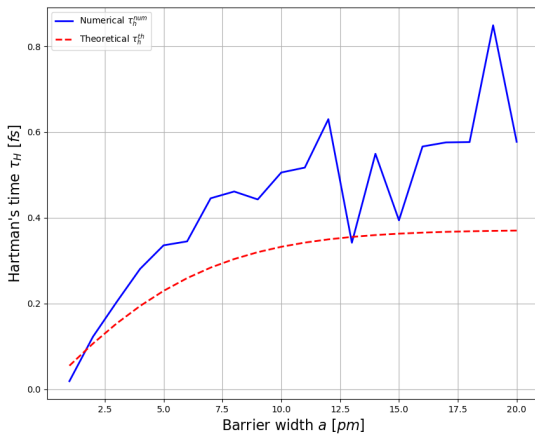


Figure 14: Theoretical and numerical Hartman effect in 2D.

However, due to the number of points involved (2000 along  $x$  in 1D and 260 along  $x$  in 2D with a grid resolution of  $260 \times 260$ ), the precision is significantly reduced, although the computational speed improves. It's also possible that my code is incorrect or not optimised enough to deduce the times from the averages (whose method relies on finding zero derivatives, so if the  $\langle x \rangle$  curve is notched, it makes the time difference we're looking for rather imprecise).

And as before, we observe a trend but not values with high precision due certainly due to numerical limitations. This demonstrates that the simulations are highly sensitive to the number of points used. The relative error remains around 40%, depending on the value. To improve accuracy, we plot the correlation graph, including the  $R^2$  coefficient, as shown in Fig.16:

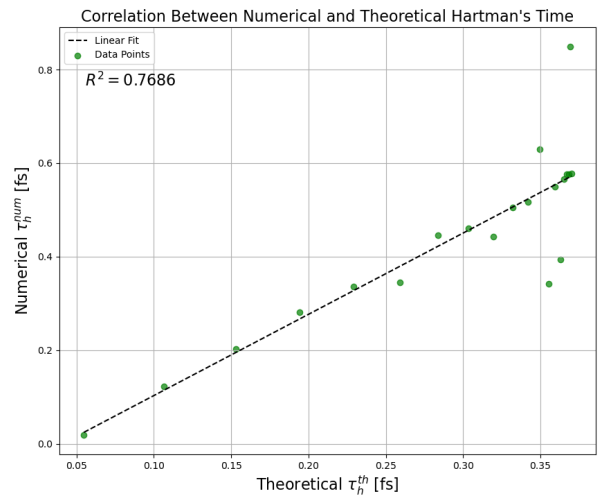


Figure 16: Correlation between theoretical and numerical traversal times in 2D.

As expected, the correlation graph clearly shows that the numerical data in 2D is less precise than in 1D. However, the precision is relatively good for low theoretical traversal times and deteriorates as we approach the expected convergence. The  $R^2$  value is approximately 0.77, which is acceptable but leaves room for significant improvement.

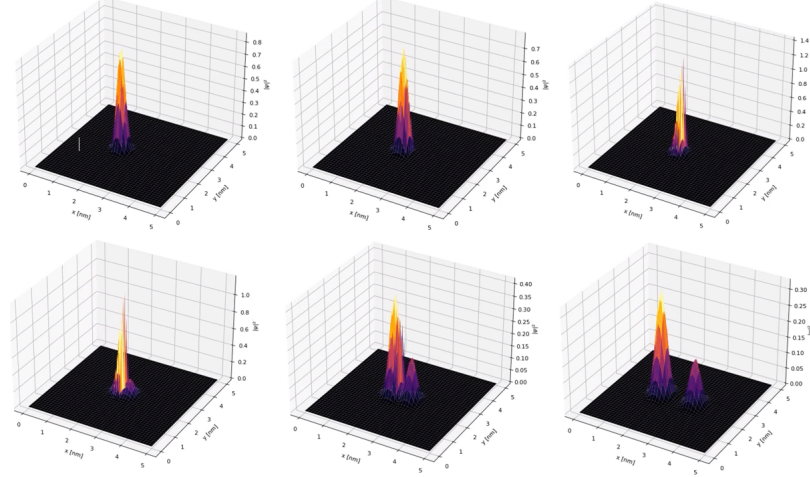


Figure 15: Simulation of the 2D tunneling effect observed at different time steps with a 3rd dimension of  $|\psi|^2$ . Animation of this figure provided in the Beta file named ‘QT\_2D\_and\_3D’.

### 4.3 Another representation of the 2D tunneling effect

This short section will present another way to represent the 2D tunneling effect using a 3D plot where the height is given by  $|\psi|^2$ . This will allow us to observe the shape of the wave function at different time steps and verify its Gaussian form. We can then compare this with the expected and simulated form shown in Fig.10.

By adding a third dimension associated with the wave function  $|\psi|^2$ , we obtain the plot shown in Fig.15.

Once again, we can observe the quantum nature of the system through the discretization of the values of  $\psi^2$  before crossing the barrier. Afterward, we notice two Gaussian profiles on the left and right, highlighting the quantum tunneling effect: a non-zero probability of crossing a barrier with a potential higher than the particle’s energy.

### 4.4 Conclusion

The analysis of the **Beta** part shows that the data obtained from the numerical simulations correspond relatively well with the theoretical values, although there is no very precise correspondence. This could be explained by edge effects where the wave function bounces and interacts with itself or by the numerical resolution not being good enough which introduces unwanted variations in our results.

## 5 Golden part - The Quantum Double Slit Experiment

The Double Slit Experiment is one of the most famous and intriguing experiments in quantum mechanics. It demonstrates the wave-particle duality of quantum objects<sup>5</sup>, a fundamental aspect of quantum theory. In this experiment, particles such as electrons or photons are directed at a barrier with two slits. The particles then hit a detection screen on the other side of the barrier.

When a single particle passes through the slits, it behaves like a wave, creating an interference pattern on the screen, a phenomenon characteristic of waves even if the particles are sent one by one [7]. This suggests that each particle interferes with itself as if it were a wave.

### 5.1 Code Initialization and Numerical Resolution

In this section, we slightly modified our quantum box from Fig.9 by introducing two slits of width  $l$  separated by a distance  $d$ . The barrier width  $a$  is kept smaller than before (around 0.025 nm), and the potential height is set to  $V_0 = 1000$  eV to avoid any tunneling effect, which could interfere with the accuracy of our simulation.

<sup>5</sup>Property where quantum objects can behave both as particles and as waves

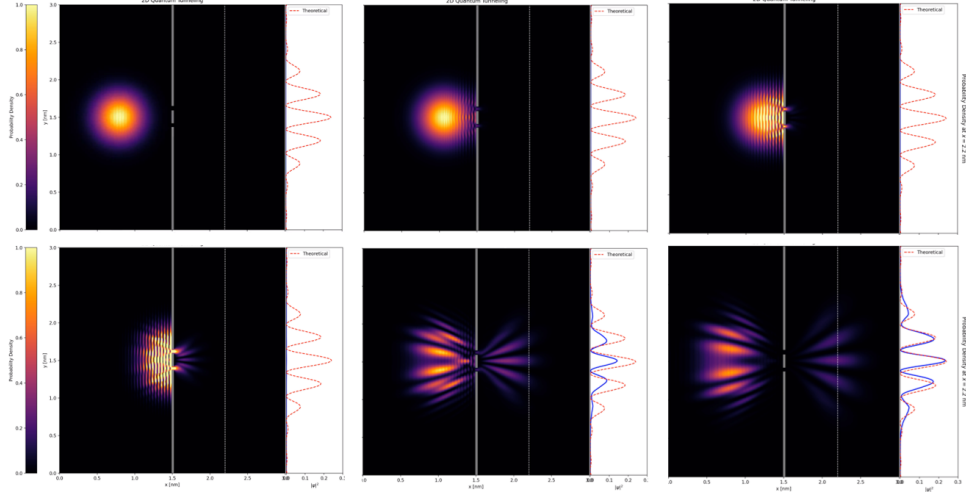


Figure 17: Simulation of the 2D double-slit experiment observed at different time steps, along with a 1D plot highlighting the interference pattern. An animation of this figure is provided in the Gold file named ‘DSE2D’.

The box then takes the shape shown in Fig. 18 and the Gaussian wave packet is the same as the one defined in Eq. (31), since we are still working in the 2D case.

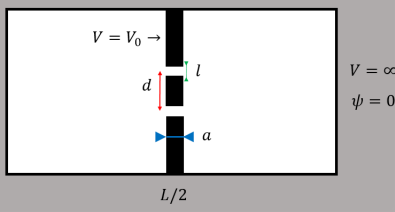


Figure 18: Quantum box used in the double-slit experiment inspired by Young’s setup.

The potential is then defined numerically as follows:

```

U0 = 1e3 # Potential in eV
a = 2.5e-11 # Barrier width
l = 5e-11 # Slit width
d = 2.3e-10 # Distance between slits
center_x, center_y = Lx / 2, Ly / 2
# Center of the barrier

# Calculating slit positions
upper_slit_bottom = center_y + d/2 + 1/2
# Bottom of upper slit

lower_slit_top = center_y - d/2 - 1/2
# Top of lower slit

```

```

# Definition of the potential U with np.where
U = np.where((X >= center_x - a / 2) &
              (X <= center_x + a / 2) # Barrier
              & ~(((Y >= upper_slit_bottom - 1) &
                    (Y <= upper_slit_bottom))
                  | ((Y >= lower_slit_top) &
                    (Y <= lower_slit_top + 1))), U0, 0)

```

We also include a 1D plot of the shape of  $|\psi|^2$  at the distance  $D = 2.2$  nm, as in Fig. 10. This gives us the result shown in Fig. 17.

In this graph, we observe how the wave function progressively develops wave-like behavior as it passes through the double slits, resulting in an interference pattern.

However, we notice that the interference pattern does not perfectly match the theoretical curve (red) compared to the numerical results (blue), especially at the edges of the graph. This discrepancy may arise from boundary effects caused by the finite size of the box.

Despite this limitation, we can still analyze and compare some aspects of this experiment from both numerical and theoretical perspectives.

## 5.2 Coherence and Validity of the Simulation

The double-slit experiment is linked to the phenomenon of interference (quantum or optical) [9, 11], which we study in this section along with the concept of diffraction.

The interference pattern, meaning the light intensity observed on a screen, is described by Eq. (32):

$$I(x) = I_0 \operatorname{sinc}^2\left(\frac{\pi x}{i}\right) \cos^2\left(\pi \frac{x}{L_d}\right) \quad (32)$$

Here, the  $\operatorname{sinc}^2$  term represents diffraction, while the  $\cos^2$  term represents interference. We can see this in the Fig.19 where the  $\operatorname{sinc}^2$  represents the signal envelope.

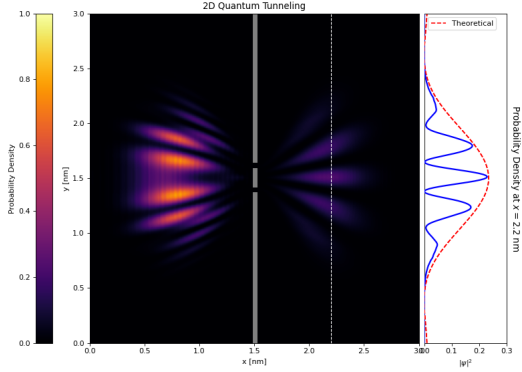


Figure 19: Intensity of the signal representing the interference (blue, obtained digitally) compared with the envelope representing the diffraction of the wave

In the Eq.(32), the parameter  $i$  corresponds to the fringe spacing, defined by Eq. (33):

$$i = \frac{\lambda D}{d} \quad (33)$$

where  $d$  is the distance between the two slits,  $\lambda$  is the wavelength, and  $D$  is the distance between the slits and the screen.

$L_d$  corresponds to the width of the diffraction pattern, defined by Eq. (34):

$$L_d = \frac{\lambda D}{l} \quad (34)$$

where  $l$  is the width of a single slit.

More precisely, in quantum mechanics, Young's double-slit experiment involves the superposition property of the wave function (derived from Eq.(6)). This

means a particle can pass through both slits simultaneously, creating visible interference patterns<sup>6</sup> via the wave function, as shown in Fig.17.

### 5.2.1 Study of $\lambda$ Dependence on Fringe Spacing

The interference patterns allow us to observe fringe spacings [11], as defined by Eq. (33).

We aim to study the size of the fringe spacing  $i$  based on the parameters it depends on. For this, we use the numerical tool `find_peaks`, which can detect peaks in a signal. From these peaks, we calculate the distance between two consecutive ones. To improve accuracy, the total length covered by the largest number of peaks was divided by the number of peaks.

To verify whether the dependence on  $\lambda$  is linear, we analyze several wavelength values and study their impact on fringe spacing.

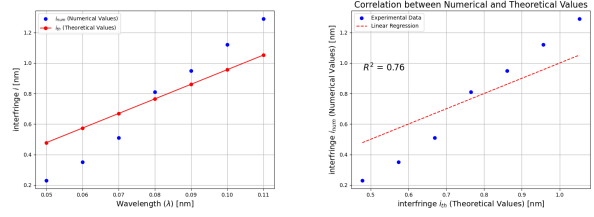


Figure 20:  $i_{th}$  and  $i_{num}$  as functions of  $\lambda$  (left). Correlation plot between  $i_{th}$  and  $i_{num}$  showing  $R^2 = 0.76$

From Fig. 20, we observe a clear linear trend in the measured fringe spacing  $i$ . However, it does not perfectly match the theoretical linear trend.

The correlation coefficient  $R^2 = 0.76$  indicates significant discrepancies between the theoretical and numerical values.

These discrepancies might be explained by boundary effects that allow the wave function to bounce and interact with itself. Additionally, numerical effects similar to those observed in Fig.14 in the previous section could also play a role.

<sup>6</sup>In reality, the wave function itself is not directly observable because a measurement collapses the wave function. However, the interference pattern can be reconstructed by performing multiple measurements [2].

### 5.2.2 Study of $D$ Dependence on Fringe Spacing

We now analyze the dependence of the fringe spacing  $i$  on the distance  $D$  between the slits and the observer<sup>7</sup>.

As with  $\lambda$ , we expect a linear relationship between the distance  $D$  and the fringe spacing  $i$ . To test this, we compute  $i$  for several values of  $D$  (limited by the size of the quantum box) using the numerical peak detection method. The results are shown in Fig. 21.

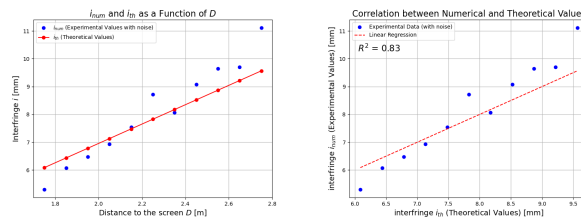


Figure 21:  $i_{th}$  and  $i_{num}$  as functions of the distance  $D$  (left). Correlation plot between  $i_{th}$  and  $i_{num}$  showing  $R^2 = 0.83$ .

From Fig. 21, we observe a much better linear trend compared to  $\lambda$  in Fig. 20, although it is still not perfect.

The improved linear trend, reflected in the higher  $R^2$  value of 0.83, might be due to the fact that  $D$  directly influences only the fringe spacing, whereas  $\lambda$  also plays a role in establishing the energy as given by Eq.(18).

This greater involvement of  $\lambda$  in the simulation contributes to more significant variations in the results compared to  $D$ , even though both quantities exhibit a linear dependence in Eq.(33).

### 5.2.3 Study of the Dependence of Slit Distance $d$ on Fringe Spacing

Finally, we analyze the effect of the slit separation  $d$  on the fringe spacing  $i$ , which is inversely proportional to  $d$  (Eq.(33)).

For different values of  $d$ , we compute the numerical fringe spacing  $i_{num}$  using the peak detection method.

The results are shown in Fig.22.

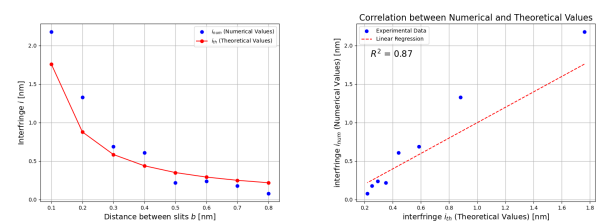


Figure 22:  $i_{th}$  and  $i_{num}$  as functions of the slit separation  $d$  (left). Correlation plot between  $i_{th}$  and  $i_{num}$  showing  $R^2 = 0.87$ .

We observe an almost  $d^{-1}$  trend, as indicated by the  $R^2 = 0.87$  in the correlation graph.

This relatively high value compared to that obtained for  $\lambda$  can be attributed to similar reasons as those for  $D$ . Specifically, the simulation itself does not directly depend on the slit separation, so variations in  $d$  have a smaller impact on the output and the numerical determination of  $i_{num}$ .

However, it is also possible that boundary effects or numerical integration inaccuracies contribute to the slight deviation from the theoretical trend.

### 5.2.4 Study of the Diffraction Pattern

Having focused on interference patterns, we now turn our attention to diffraction patterns. According to Eq. (32), the parameters  $\lambda$  and  $D$  have already been studied and do not require further analysis. However, we can investigate the influence of the slit width  $l$  on the diffraction spot size  $L_d$ .

Similar to the study of fringe spacing, we theoretically plot  $L_d$  for several values of  $l$  (avoiding values that are too large or too small to prevent incoherent results, which are discarded from the analysis). Numerically, instead of measuring the distance between two peaks, we determine the distance between two nodes ( $I(x) = 0$ ). The results are presented in Fig.24.

<sup>7</sup>Numerically, the observer corresponds to a condition, but in reality, it represents a screen or a detector

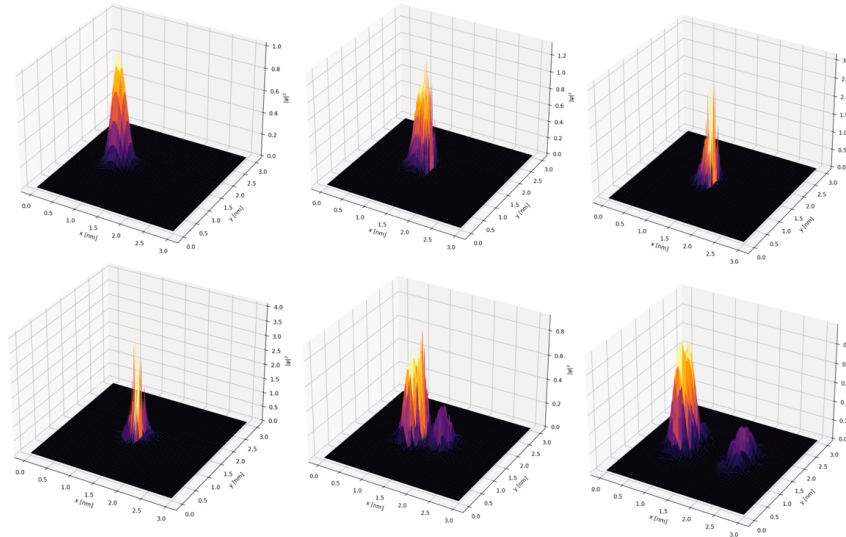


Figure 23: Simulation of the 2D double-slit experiment observed at different time steps in a 3rd dimension of  $|\psi|^2$ . An animation of this figure is provided in the Gold file named ‘DSE2D+3D’.

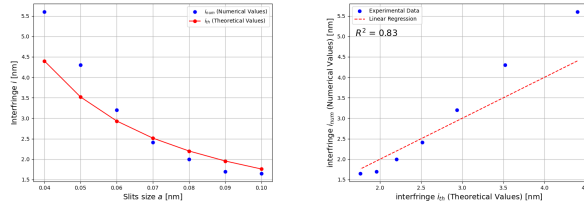


Figure 24:  $L_d^{\text{th}}$  and  $L_d^{\text{num}}$  as functions of the slit width  $l$  (left). Correlation plot between  $L_d^{\text{th}}$  and  $L_d^{\text{num}}$  showing  $R^2 = 0.83$ .

We observe a trend similar to that found in the study of the slit separation  $d$  for fringe spacing. Here, the relationship exhibits an approximately  $l^{-1}$  dependence, corroborated by an  $R^2 = 0.83$ . This value is very close to the  $R^2$  obtained for  $d$  because the dependencies and analysis are quite similar.

The discrepancies can be explained by the same arguments: increasing the simulation box size and using a finer grid would likely improve the numerical data. However, this would significantly increase the computational time.

### 5.3 Alternative Representation of the Double-Slit with an Additional Dimension

This brief section introduces an alternative way to visualize the Young double-slit experiment numerically, similar to the 2D tunneling effect, by employing a 3D

plot where the height represents the magnitude  $|\psi|^2$ . This corresponds to Fig.23.

By comparing the results of this simulation with those in Fig.17, we can further analyze the probabilistic and wave-like nature of the wave function associated with a particle, thereby illustrating the wave-particle duality of quantum mechanics.

The probability wave passing through the slits exhibits a shape consistent with the theoretical expectations described by Eq.(32).

### 5.4 Conclusion

The numerical study of the double-slit experiment successfully demonstrates the wave-particle duality by reproducing the expected interference and diffraction patterns. However the dependence of different parameters such as wavelength  $\lambda$ , slit separation  $d$  or screen distance  $D$  on the interfringe and diffraction features do not align perfectly with theoretical predictions. These discrepancies could highlight the impact of numerical limitations.

## 6 Platinum Part - Customizable 2D Potentials

This optional section explores customizable 2D potentials. After studying two different potentials in the **Beta** and **Gold** versions, it seemed interesting to test the nu-

merical simulation on potentials that we can customize ourselves.

## 6.1 Potentials from a Drawing

One of the customization options for the potential is to illustrate it by literally drawing it.

However, since the 2D numerical simulations work fairly well, we will not analyze this section in detail, as it can be considered valid but more of an artifact for two reasons. The first reason is that studying "random" or hand-drawn potentials would be too complex, as there is no analytical expression to describe them. Furthermore, it would make this report, which is already quite detailed and comprehensive, significantly longer.

When running the code, a blank window appears where you can draw the shape of your choice. Once done, you need to confirm the drawing by pressing **Enter**, and you will then get the potential corresponding to your drawing, as shown in Fig.25.

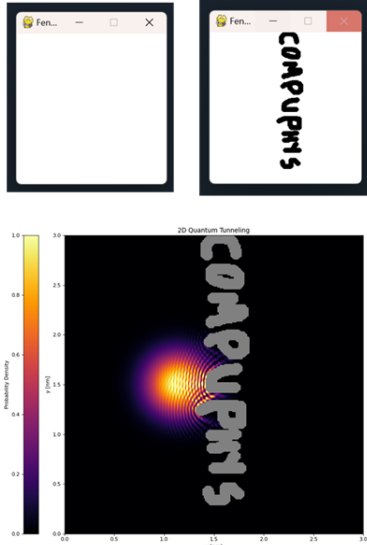


Figure 25: Simulation of a Gaussian wave packet interacting with a potential in **CompuPhys**

In Fig.25, we can see that even though the potential is random, quantum behavior starts to emerge due to the interaction between the Gaussian wave packet and the **CompuPhys** potential. This at least suggests that the results are not to be immediately dismissed, even though more detailed analysis would be necessary.

## 6.2 Potentials from an Image

Drawing the potential is fun but not very precise, so it can be improved by importing images. If a potential is described by a specific configuration in the form of an image, it becomes practical to import it (as long as the image size matches the resolution of the grid used for the simulation).

The imported image must be in black and white, flipped, rotated by an angle of  $\pi/2$ , and in **.bmp** format, as shown in Fig.26 (although with more time, it would be possible to address the flip and rotation issues).

In the code, the image should be imported by specifying its filename. When the code is run, a blank window appears as in Fig.25, but instead of drawing anything, you press **Enter** directly, and the image is converted into the potential, as shown in Fig.26. The potential in this example is called "*Potentiel de Noyelles*".

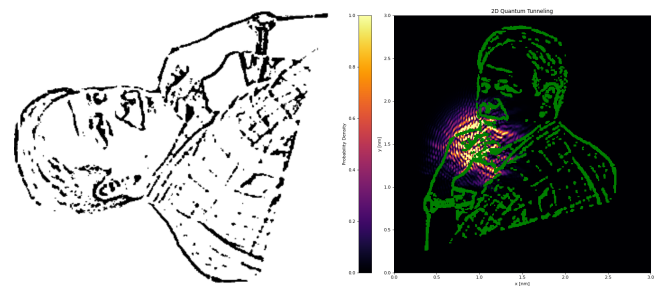


Figure 26: "*Potentiel de Noyelles*" represented as an image (left) and the simulation of a Gaussian wave packet interacting with the "*Potentiel de Noyelles*" (right).

Beyond this, further studies or refinements of this method could be considered. For instance, one might explore its application to quantum gases instead of a quantum box or even investigate harmonic potentials depending on the potential usefulness of this approach.

## 7 Acknowledgements

I would like to thank my classmate Léo BECHET from the Master 2 CompuPhys for suggesting the idea of a **Platinum** part, where I was able to code the drawn potential. I also thank him for his help in implementing the feature to generate a potential from an image.

## 8 Conclusion

This study focused on numerical simulations of quantum phenomena like tunneling, the double-slit experiment, and customizable 2D potentials.

The **Alpha** part confirmed that the tunneling simulations matched theoretical predictions well, validating the model. In the **Beta** part, the results were close to theory but showed small deviations due to edge effects and limited resolution. The **Gold** part successfully reproduced interference and diffraction patterns in the double-slit experiment, demonstrating wave-particle duality, though some differences with theory were noted.

Overall, the simulations worked well and showed the potential of numerical methods in quantum mechanics. The **Platinum** part opens up new possibilities for testing more complex potentials in the future.

## References

- [1] Muhammad Adeel Ajaib. Numerical methods and causality in physics. *arXiv preprint arXiv:1302.5601*, 2013.
- [2] Roger Bach, Damian Pope, Sy-Hwang Liou, and Herman Batelaan. Controlled double-slit electron diffraction. *New Journal of Physics*, 15(3):033018, 2013.
- [3] Raymond Y Chiao and Aephraim M Steinberg. Vi: tunneling times and superluminality. In *Progress in Optics*, volume 37, pages 345–405. Elsevier, 1997.
- [4] Paul Charles William Davies. Quantum tunneling time. *American journal of physics*, 73(1):23–27, 2005.
- [5] Thomas E Hartman. Tunneling of a wave packet. *Journal of Applied Physics*, 33(12):3427–3433, 1962.
- [6] J Jakiel, VS Olkhovsky, and E Recami. The validity of the hartman effect for all kinds of mean tunnelling times. In *AIP Conference Proceedings*, volume 461, pages 299–302. American Institute of Physics, 1999.
- [7] Manpreet Kaur and Mandip Singh. Quantum double-double-slit experiment with momentum entangled photons. *Scientific Reports*, 10(1):11427, 2020.
- [8] J Kiukas, A Ruschhaupt, and RF Werner. Tunneling times with covariant measurements. *Foundations of Physics*, 39:829–846, 2009.
- [9] Hui Peng. Experimental study of mystery of double slit—comprehensive double slit experiments. *International Journal of Physics*, 9(2):114–127, 2021.
- [10] Mohsen Razavy. *Quantum theory of tunneling*. World Scientific, 2013.
- [11] Richard Rolleigh. The double slit experiment and quantum mechanics. *Hendrix College Faculty Archives*, 2014.
- [12] Jorge Henrique Sales, Alfredo Takashi Suzuki, and Daykson N Possidonio. Quantum tunneling time in the light-front. *Light Cone 2019-QCD on the Light Cone: From Hadrons to Heavy Ions*, page 91, 2019.